TUDelft

Delft University of Technology

Parametrizing nonlinearity in orbital velocity at fetch-limited, low-energy beaches

van der Lugt, M. A.; de Schipper, M. A.; Reniers, A. J.H.M.; Ruessink, B. G.

Citation (APA)
van der Lugt, M. A., de Schipper, M. A., Reniers, A. J. H. M., & Ruessink, B. G. (2024). Parametrizing nonlinearity in orbital velocity at fetch-limited, low-energy beaches. *Coastal Engineering*, *194*, Article 104602. https://doi.org/10.1016/j.coastaleng.2024.104602

Important note
To cite this publication, please use the final published version (if applicable).
Please check the document version above.

Parametrizing nonlinearity in orbital velocity at fetch-limited, low-energy beaches

M.A. van der Lugt [a,b,*], M.A. de Schipper [a], A.J.H.M. Reniers [a], B.G. Ruessink [c]

[a] *Department of Hydraulic Engineering, Fac. of Civil Engineering, TU Delft, P.O. Box 5048, 2600 GA Delft, The Netherlands*
[b] *Department of Applied Morphodynamics, Deltares, P.O. Box 177, 2600 MH Delft, The Netherlands*
[c] *Department of Physical Geography, Fac. of Geosciences, Utrecht University, P.O. Box 80.115, 3508 TC Utrecht, The Netherlands*

ARTICLE INFO

ABSTRACT

Wave nonlinearity plays an important role in cross-shore beach morphodynamics and is often parameterized in engineering-type morphodynamic models through a nonlinear relationship with the Ursell number. It is not evident that the relationship established in previous studies also holds for sheltered sites with fetch-limited seas as they are more prone to effects of local winds and currents, the waves are generally steeper, and the beaches are typically reflective. This study investigates near-bed orbital velocity nonlinearity from wave records collected at two sheltered beaches in The Netherlands and contrasts them to earlier observations made along the exposed, wave-dominated North Sea coast. Our observations at sheltered beaches show that the Ursell number has comparable skill in predicting wave nonlinearity as it has on previously studied exposed coasts. However, the orbital velocities at sheltered coasts are more asymmetric for the same Ursell number than on exposed coasts. When exposed coast data were examined for moments with comparable high-steepness waves, a similar effect on asymmetry was observed. In addition, following and opposing winds were found to have a clear relationship with total nonlinearity, while they did not affect the phase between skewness and asymmetry at the sheltered beaches. Refitting the free parameters of an Ursell-based predictor improved the bias for the asymmetry parameterization. Whether this has implications for modeling of the magnitude of wave-nonlinearity-driven sediment transport using engineering type models is strongly dependent on the sediment transport formulation used, as these formulations depend on additional calibration coefficients too.

1. Introduction

Sandy sheltered coastlines are found in estuaries, coastal basins and inland lakes. Because they are not as dynamic as exposed coasts, they have received less attention. Nevertheless, these sheltered beaches also protect vital coastal infrastructure and communities rely on these beaches as a defence against flooding (Vila-Concejo et al., 2020; Fellowes et al., 2021). Understanding the hydrodynamics that drive the dynamics of sandy beaches at sheltered coastlines is therefore important.

Process-based morphodynamic models are used as design tools for coastal nourishments, and they are now increasingly used for coastal engineering of sandy foreshores in sheltered regions too (Perk et al., 2019; Ton et al., 2021). These models rely on a sound description of the relevant physical processes and generally resolve wave-driven sediment transport in a phase-averaged, spectral approach. One process relevant for the cross-shore sediment balance is the transport by wave nonlinearity. As waves propagate from deep to shallow water, their surface signature deforms, first by becoming skewed, and with decreasing

water depth turning asymmetric whereafter they eventually break (e.g. Elgar and Guza, 1985). The orbital velocity underneath these surface waves changes analogously. In the lower part of the free stream, close to the bottom boundary layer where sediment is in suspension, wave nonlinearity can drive a shoreward sediment flux (Hoefel and Elgar, 2003; Hsu et al., 2006). From a Bagnold's type energetics-based sediment transport model ($S_T \sim \langle u^3 \rangle$, with S_T a measure of total transport, u the total velocity signal and the angle brackets representing an average over many waves Bailard and Inman, 1981), it is evident that orbital velocity skewness

$$S_u = \langle u_{orb}^3 \rangle / SD(u_{orb})^3 \qquad (1)$$

(u_{orb} being the orbital component of u, and SD for standard deviation) holds a direct relation to the sediment transport rate. Early attempts to incorporate wave nonlinearity in phase-averaged morphodynamic models therefore focused on parametrizing orbital velocity skewness S_u from local phase-averaged wave statistics. Later, it was shown that

---

including velocity asymmetry (acceleration skewness)

$$A_u = \langle \mathcal{H}(u_{orb})^3 \rangle / SD(u_{orb})^3 \qquad (2)$$

with $\mathcal{H}$ the Hilbert transform, is important as well (Drake and Calantoni, 2001; Henderson et al., 2004).

The sediment transport equations (e.g. Van der A et al., 2013; Van Rijn, 2007; van Thiel de Vries, 2009) used in common process-based models (e.g. Lesser et al., 2004; Warner et al., 2008; Roelvink et al., 2009) parametrize S_u and A_u based on the nondimensional Ursell number

$$Ur = \frac{3}{8} \frac{H_{m0} k}{(kd)^3} \qquad (3)$$

with significant wave height H_{m0}, wave number k and local water depth d.

The relations between S_u and A_u and Ur that are most commonly applied were derived in Ruessink et al. (2012) from a large dataset of field observations at mild-sloping beaches. Their parameterization (RRvR12) built upon the work of Doering and Bowen (1995) by extending the range of the database of field observations into higher Ursell numbers with wave records from 11 field campaigns undertaken along the low-sloping, high-energy exposed Dutch and French coast. From the extended database, they identified an upper bound for the total wave nonlinearity $B = \sqrt{S_u^2 + A_u^2}$ that could not be deduced yet by Doering and Bowen (1995). The RRvR12 predictor for skewness S_u and asymmetry A_u reads:

$$S_u = B \cos(\Psi) \qquad (4)$$

$$A_u = B \sin(\Psi) \qquad (5)$$

with total nonlinearity B and phase Ψ empirically derived as:

$$B = \frac{p_2 - p_1}{1 + \exp(\frac{p_3 - \log(Ur)}{p_4})} \qquad (6)$$

$$\Psi = -90° + 90° \tanh(p_5/Ur^{p_6}) \qquad (7)$$

The free parameters p_2-p_6 were obtained by fitting a Boltzmann sigmoid with 3 degrees of freedom and a $\tanh$ function with 2 degrees of freedom to their database. p_1 was set to 0 from the theoretical consideration that in deep water ($Ur \to 0$), the waves are fully linear. p_2 describes an upper bound to B when $Ur \to \infty$.

The sea state is expected to differ considerably between sheltered and exposed coasts. First of all, the sea state at sheltered beaches is less energetic. This results in less transport capacity by waves alone and therefore, wind- or tidally driven currents could have a relatively larger impact on sediment transport. Following or opposing currents can change the shape of surface waves, and depending on their relative strength ($c/\bar{u}$ with $\bar{u}$ the mean current and c the phase celerity) affect the orbital velocity nonlinearity as experienced by the bed (De Wit et al., 2019). Sheltered beach sea states are often locally generated under fetch-limited conditions, resulting in short wave period and small phase celerity c, suggesting that currents play a larger role in wave shape. Moreover, wave age c/u_w^* with u_w^* the wind shear velocity generally is small at sheltered locations. Consequently, the sea state is younger and wave fields are therefore expected to be steeper and have a wider directional spread as well as a more gradual decay of energy with frequency (Donelan et al., 1985; Young et al., 1996; Ewans, 1998). Broad-bandedness was shown to negatively affect wave nonlinearity (Rocha et al., 2017). Directional spread has been regarded as the dominant difference in observed wave nonlinearity in lab conditions compared to field conditions, thereby affecting the strength of the nonlinearity (Ruessink et al., 2012). Another effect of the fetch-limited conditions and corresponding small wave age at sheltered beaches is that the sea state is strongly tied to local winds. In laboratory experiments inverse wave age was shown to relate strongly with velocity asymmetry (Leykin et al., 1995), and following and opposing winds were found to affect the development of both skewness

and asymmetry for shoaling waves (Feddersen and Veron, 2005). Last, low-energy beaches are generally characterized by a steep, reflective beach face (Jackson et al., 2002). Reflective beaches were not part of the calibration database for RRvR12, but Filipot (2015) showed, using numerical experiments, that steep foreshore slopes negatively affect wave nonlinearity.

Considering the expected differences between sea states at sheltered and exposed coasts, it is not evident that local integral wave statistics capture the near-bed velocity nonlinearity well nor that the skill of the RRvR12 parameterization for predicting near-bed velocity nonlinearity is similar when used at sheltered beaches. Understanding how A_u and S_u develop along sheltered coastlines is important to validate the typical modelling approach for predicting their beach profile. To that end, this study examines observations of wave nonlinearity from low-energy beaches and studies dependence on the sea state. From these observations, we evaluate the appropriateness of the Ursell number to predict S_u and A_u in low-energy environments and assesses the skill of the RRvR12 predictor for use at sheltered beaches.

2. Methodology

2.1. Approach

We analyzed wave records from two low-energy beaches in the Netherlands (Fig. 1a). The first is a lake beach, where tides are inherently absent and all waves are locally generated over constant water depth of approximately 2 m (Fig. 1b, d). The sea state at this beach comprises of only truly locally generated low-energy waves. The second is a back-barrier beach (Fig. 1c, e) with tidal excursion and waves that are predominantly locally generated over the basin bathymetry of varying depths, but where a limited amount of North Sea waves can propagate into the basin too through a tidal inlet. This second site, sheltered from the open ocean but with similar tidal excursions, can be considered as a low-energy site bridging the gap between the dissipative exposed coasts studied in the wave shape literature in the field and the fetch-limited lakeside case. The shoreline orientation of the back-barrier beach with respect to the dominant prevailing wind direction (SSW) allows analysis of the effect of local wind forcing on wave nonlinearity.

The underlying approach to our methodology was to follow the data processing steps exactly as outlined in Ruessink et al. (2012) to enable a proper comparison between our low-energy observations and their exposed coast observations. This implies that wave shape in our work refers to velocity nonlinearity found in timeseries without translation of the recorded signals to other heights within the water column. This is in contrast with works that study wave nonlinearity by analysis of sea-surface reconstructions from pressure sensors (De Wit et al., 2019; Rocha et al., 2013), or compute wave nonlinearity from a wave-by-wave approach (Kalra et al., 2022).

2.2. Field campaigns

The lakeside field site is situated along the Houtribdijk, which divides the Markermeer and the IJsselmeer. The maximum fetch is 40 km along the lake for wind from the South-southwest (Fig. 1b). Water level is actively managed and varies from winter to summer by a few decimetres. Ambient currents are expected to be driven by large-scale circulation in the entire lake basin as a result of the wind forcing and the basin geometry (Ton et al., 2021). The measurements at this site were part of the 19-month measurement campaign of the LakeSide project (Ton, 2023). Three ADV stations from a cross-shore array were selected for further analysis (Fig. 1d). The most offshore (at 0.8 m above the bed) and most onshore ADV (at 0.3 m above the bed) measured continuously between October 2019 and February 2021. The central ADV recorded between January 2020 and February 2021 (at 0.8 m above the bed). These ADV's recorded continuously at 4 Hz.
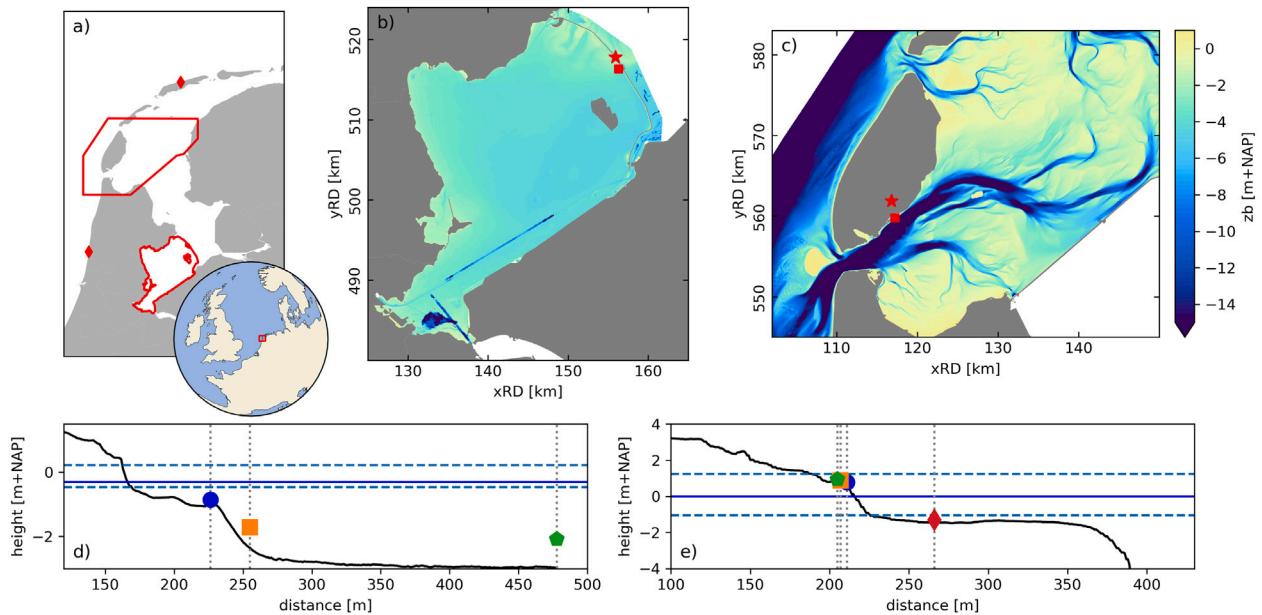
Fig. 1. Geographical location of analysed low-energy ADV stations. (a) Location of studied sheltered field sites along the Dutch coast in red outlines, red diamonds indicate locations of open coast sites discussed. (b) Geometry and bathymetry of the Markermeer for the lakeside beach. Bathymetry displayed in the local datum NAP, approximately equal to mean sea level. (c), Geometry and bathymetry of the Marsdiep basin for the back-barrier beach. Both in panel (b) and (c): Red dot marks location of cross-shore arrays while red star indicates the location of nearby weather station. Topography not shown; grey patches indicate land. (d) Cross-shore profile of the lakeside beach. (e) Cross-shore profile of the back-barrier beach. In (d) and (e) a solid blue line indicates mean water level and dashed lines minimum and maximum observed water levels during the measuring period. Markers indicate position and elevation of ADV stations.

The back-barrier beach is located within the Marsdiep Wadden Sea basin (Fig. 1c). Incoming waves are predominantly locally generated over a fetch of 25 km at most. Additionally, with south-westerly winds, waves generated in the North Sea can propagate through the tidal inlet and refract toward the beach. The tide in the Marsdiep basin is semi-diurnal with an average tidal amplitude of 0.7 m. The beach is situated on a submerged tidal flat adjacent to a deep tidal channel, leading to a modulation of the wave height at the beach toe with the tide. Currents are expected to be driven by the tide and at times superimposed by wind-driven currents at the basin scale (Duran-Matute et al., 2016). Along this beach and on the platform, velocity measurements were collected as part of the SEDMEX campaign between September 10 and October 18, 2021 (Van der Lugt et al., 2024). We focus on four ADVs out of the SEDMEX dataset that measured on different positions along the cross-shore profile (Fig. 1e). Sampling frequency was 16 Hz and these ADVs were positioned approximately 0.2 m above the bed.

2.3. Data processing

The ADVs recorded near-continuously pressure and velocity in 3 dimensions. These signals were cut into blocks of 10 min for analysis. See Fig. 2 for two example snapshots of time series within the dataset at energetic, nonlinear moments in time. All blocks in which the pressure sensor or the acoustic transducer fell dry were removed from the analysis. Consequently, there are no observations from the swash zone. For the most landward ADVs on the back-barrier beach, observations were available during high water only (495 blocks of 10 min).

2.3.1. Velocity skewness and asymmetry

Typically, sea-swell orbital velocity skewness and asymmetry is computed from the band-passed velocity signal in the frequency range $[0.05–f_{Nyq}]$ Hz, with f_{Nyq} the Nyquist frequency. As our observations are fetch-limited, the peak frequency is relatively large and consequently the sea-swell range is better described with a frequency range scaling with the peak frequency $[0.5f_p–f_{Nyq}]$. Therefore, for our sheltered beach wave records, orbital velocity skewness and asymmetry were calculated from 10-min velocity records using Eqs. (1) and (2)
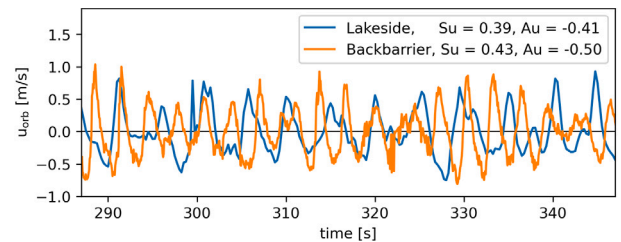

Fig. 2. Example snapshots of time series of orbital velocity in the wave direction, one for each field site. Both snapshots were taken from an energetic wave record where wave nonlinearity was present.

with u_{orb} the instantaneous velocity signal in the mean wave direction band-pass filtered to $[0.5f_p–f_{Nyq}]$.

2.3.2. Wave statistics

Spectra were calculated from 10-min (592 s) pressure blocks, each divided into 35 Hanning-windowed subblocks with a length of 32 s and using 50% overlap. These 35 individual spectra were averaged, resulting in a spectrum for each pressure block with a frequency resolution of $1/32 = 0.03125$ Hz. From the pressure measurements, we estimated block-averaged water depths and using linear wave theory, we reconstructed the spectral significant wave height $H_{m0} = 4\sqrt{m_0}$, peak frequency f_p and mean wave period $T_{m-1,0} = \frac{m_{-1}}{m_0}$ in the frequency range [0.05–1.0] Hz from the near-bed pressure signal:

$$P_{ss} = S_w^2 P_{hydrostatic} \tag{8}$$

$$S_w = \frac{\cosh(kd)}{\cosh(kh)} \tag{9}$$

with P_{ss} the variance density spectrum of the sea surface, $P_{hydrostatic}$ the variance density of the hydrostatic surface elevation, h instrument height above the bed. To prevent blow-up of noise in the power spectrum within the integration range, the linear transfer function, S_w was capped to a maximum of $S_w = \max(S_w, 5)$, as discussed in Van der Lugt et al. (2024).

The mean wave direction was analysed with two methodologies. First, as all our sheltered beach observations consist of co-located pressure and velocity recordings, we could reconstruct 2D wave spectra using the Maximum Entropy Method (MEM) (Lygre and Krogstadt, 1986) from the coupled pressure and horizontal velocity records. Mean wave direction was extracted from these 2D wave spectra following Kuik et al. (1988). Although directional spread can also be computed from the 2D spectra, we followed Ruessink et al. (2012) to compute the directional spread (S_θ) from a principal component analysis (PCA) of the 2D horizontal orbital velocity signal. In this approach, wave direction is determined by the angle of the principle axis $u_{orb,1}$ to North, and the directional spread is computed as $\tan^{-1}(u_{orb,2}, u_{orb,1})$ where $u_{orb,2}$ is the orbital velocity variance in the secondary axis orthogonal to $u_{orb,1}$. The mean wave direction of the PCA is only defined on the half-circle, which means this method does not differentiate between shoreward and seaward propagating sea states. Therefore, we used the wave direction from the 2D spectra to differentiate between shoreward and offshore directed wave angles. This deviation from the Ruessink et al. (2012) approach had negligible effect, as mean wave direction estimates from PCA and MEM, projected on the half-circle, differed only $(1 \pm 7)°$ over our entire dataset.

Ambient currents could significantly affect the wave number for low-energy sea states as this effect scales with the ratio of phase velocity to flow velocity in wave direction ($\frac{c}{\overline{u}_\parallel}$). Block-mean velocity was computed and decomposed into a component in the mean wave direction ($\overline{u}_\parallel$) and one perpendicular to that ($\overline{u}_\perp$). Currents in the direction of wave propagation affect the wave number of the sea state, and the corrected wave numbers were computed following the method of Guo (2002) by iteratively solving the linear dispersion relationship

$$\omega = \sigma + k\overline{u}_\parallel = \sqrt{gk \tanh(kh)} + k\overline{u}_\parallel \tag{10}$$

with $\omega = 2\pi/T_{m-1,0}$ the absolute wave frequency, σ the relative wave frequency and g gravitational acceleration. However, the effect of the current on wave number was shown to be limited in both subsets, because the angle between waves and currents was generally large for energetic wave records. As the analysis in Ruessink et al. (2012) did not correct the wave number for currents the remaining analysis uses uncorrected wave number $k_{m-1,0}$ to compute Ur by solving Eq. (10) with $\overline{u}_\parallel = 0$. Local wave steepness was computed as

$$s_{m-1,0} = \frac{k_{-1,0}H_{m0}}{2\pi} \tag{11}$$

The spectral width of the pressure variance density was assessed through the narrow-bandedness parameter κ in the definition by (Battjes and van Vledder, 1984):

$$\kappa^2 = \frac{1}{m_0^2} \left\{ \left[\int_0^\infty E(f) \cos\left(\frac{2\pi f}{\overline{f}_o} \right) df \right]^2 \right.$$

$$\left. + \left[\int_0^\infty E(f) \sin\left(\frac{2\pi f}{\overline{f}_o} \right) df \right]^2 \right\} \tag{12}$$

with $\overline{f}_0 = \sqrt{\frac{m_2}{m_0}}$ and m_i the ith moment of the variance density E. Larger κ implies a narrower frequency distribution.

2.3.3. Wind

10-Minute average wind speed and direction was extracted from nearby weather stations at the two site. For the lakeside beach this was station 'Houtribdijk' (KNMI, 2021, located at N52.6481, E5.4006) which is part of the KNMI measurement network and for the back-barrier beach this was weather station Hoge Berg on Texel (located at N53.0422, E4.8175). The wind speed was decomposed into components perpendicular ($u_{w,\perp}$) and parallel ($u_{w,\parallel}$) to the direction of wave propagation.

2.4. Data selection

The sheltered beach dataset contains many wave records from moments with negligible wind forcing and therefore very small amplitude, low-period waves. A selection of the entire set of observations was made which is further referred to as 'Dataset Sheltered' DS.

Although the velocity records are analysed at the depth they were recorded, the associated Ursell number needs to be computed from H_{m0} and $T_{m-1,0}$ of the reconstructed sea surface. The cap on the linear transfer function S_w prevents blow-up of noise, but does not solve the problem that waves at high kd are strongly attenuated at 0.15 m above the bed. This results in unrealistically large S_w values, which are replaced by the cap value in the applied approach. As a consequence, the shape of the spectral tail is poorly resolved for frequencies above the onset of the cap f_{cap} (see Van der Lugt et al., 2024). To mitigate the sensitivity of our analysis to uncertainty in the record's associated Ursell number, all wave records where $f_{cap} < 2f_p$ or $H_{m0} < 0.1$ m were discarded (13% records remained at the lakeside beach, and 27% of records remained at the back-barrier beach, see Fig. 3). As a last step, both field sites were given equal weight in DS by randomly sampling 2000 wave records from the shallowest station at the lakeside field site, as this station was heavily overrepresented with 22 388 valid wave records while the other stations had only up to 1224 valid records (Fig. 3). This ensured a balance between lakeside (3744 samples total) and back-barrier (3266 samples total) wave records in an analysis of goodness of fit of an Ursell based predictor.

2.5. Exposed coast wave records

Data from the Nourtec experiment (Ruessink et al., 1998), the Coast3D experiments (Kroon and De Boer, 2001; Ruessink et al., 2001) and the Egmond intertidal campaign (Price and Ruessink, 2008) were used to contrast exposed coast observations to our observations from sheltered coasts. These datasets are a subset of Dutch experiments using bi-directional electromagnetic flow (EMF) meters and ADVs analysed in Ruessink et al. (2012) and provide a total of 23 621 wave records, approximately 2/3 of the total number of wave records analysed there. This data from wave-dominated North Sea beaches is used to characterize how the sea state differs between exposed and sheltered beaches, and later, to investigate how this affects wave nonlinearity. We further refer to this dataset of exposed coastal wave records as 'Dataset Exposed' DE. Wave records in DE were processed in the same way as the sheltered beach wave records.

3. Results

3.1. Sea state characterization

Lakeside and back-barrier sea states show comparable mean wave height (~0.2 m) and mean wave period (2–3 s) (Fig. 3). Significant wave height H_{m0} and mean wave period $T_{m-1,0}$ at the lakeside beach are strongly coupled (Fig. 3a). This is less so at the back-barrier beach (Fig. 3b), where both steep waves (up to 1:15 in the deep water definition $\frac{2\pi H}{gT_{m-1,0}^2}$) as well as mild ones (gentler than 1:60) are present, while lakeside ware records were always found to be steep. The upper bound to wave steepness is approximately 1:15 at the back-barrier site and 1:7 at the lakeside site. The bound of 1:7 is commonly believed to be the maximum steepness of individual waves in deep water in equilibrium (Miche, 1944).

The sea state of DS is further characterized by means of distributions of occurrence of common sea state characteristics and compared to the distribution of the exposed wave records of DE (Fig. 4). Observed mean wave period in DS is always shorter than 5 s, whereas the mean wave period in the exposed dataset is generally larger than 5 s (Fig. 4b). As a consequence, the distribution of relative water depth kd is heavier towards higher values in DS compared to DE (Fig. 4c). Local wave
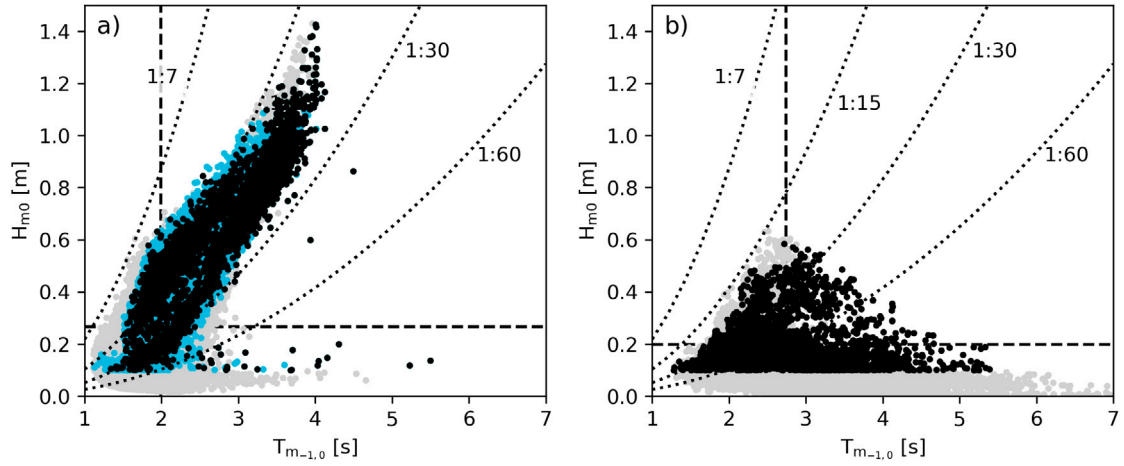
Fig. 3. Visualization of the selection of wave records for Dataset Sheltered DS through phase plane of wave height versus mean wave period. (a) Wave records from the lakeside beach, (b) Wave records from the back-barrier beach. Light grey colored wave records were discarded based on the criterion $f_{cap} < 2f_p$ or $H_{m0} < 0.1$ m, and cyan colored wave records were discarded in the downsampling of the shallow water lakeside station. Black colored wave records entail DS. Dashed lines indicate the full dataset's mean values, dotted lines indicate lines of constant deep water wave steepness.
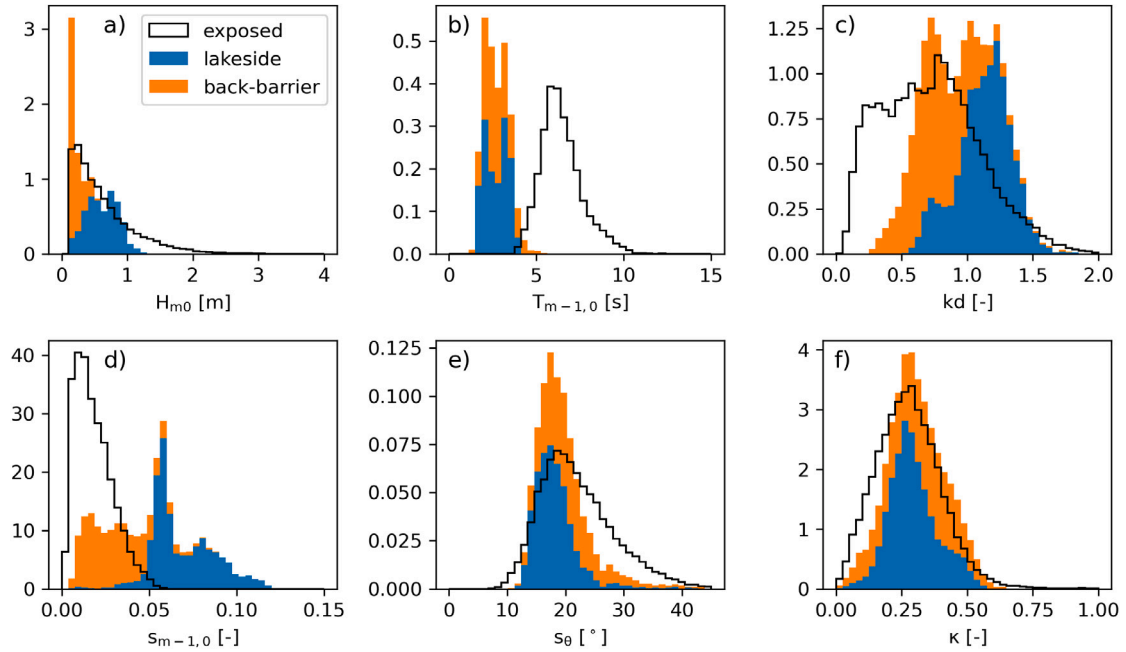

Fig. 4. Normalized (unit surface area) histograms of the sea state in DS (filled histograms, orange color indicates sea states from back-barrier site, blue color from lakeside site, normalized on the total set of sea states in DS.) with the sea state in DE for comparison (black, open). (a) Significant wave height, (b) Mean wave period $T_{m-1,0}$, (c) Relative water depth kd, (d) Local wave steepness $s_{m-1,0}$, (e) Directional spreading s_θ, (f) Spectral narrowness κ.

steepness $s_{m-1,0}$ differs strongly between exposed and sheltered datasets (Fig. 4d). The sheltered dataset shows a wide distribution of gently sloping as well as very steep wave records: $s_{m-1,0} \in [0.0-0.12]$, whereas the exposed dataset contains predominantly very mild sloping waves: $s_{m-1,0} \in [0.0-0.04]$, with the mode of the distribution at $s_{m-1,0} = 0.002$. The peak in wave steepness at $s_{m-1,0} = 0.07$ in DS originates from the two deepest stations in the lakeside dataset, for which only the most energetic wave records were retained in DS, as at other moments the relatively large water depth at these stations led to discarding based on $f_{cap} < f_p$. DS and DE both have a mean directional spreading slightly lower than $s_\theta = 20°$, but the distribution in DS is smaller than in DE, and in particular it does not contain any wave records with spreading $s_\theta \leq 10°$ (Fig. 4e). Lastly, both datasets show comparable narrow-bandedness in the frequency distribution (Fig. 4f).

3.2. Ursell number as predictor of S_u and A_u

Our dataset DS contains observations up to an Ursell number of $\mathcal{O}(1)$ (Fig. 5). In line with the RRvR12 predictor, velocity skewness tends to be positive for $Ur > 0.1$ (Fig. 5a) and was observed to a maximum of $S_u \sim 0.5$. Velocity asymmetry tends to be negative for increasing Ursell number, reaching $A_u \sim -0.5$ at around $Ur = 1$. However, the onset of this trend appears at a lower Ursell number than in the RRvR12 predictor (Fig. 5c). Wave records from the lakeside beach tend to have slightly larger S_u than from the back-barrier beach (Fig. 5b), while there is no such separation for A_u (Fig. 5d).

The spread of wave records on the $A_u - Ur$ and $S_u - Ur$ phase planes of DS falls within the observed spread of exposed wave records (Ruessink et al., 2012, their Figure 1), but the Ursell-based parameterization describes only the evolution of the general trend. The free parameters in this predictor describe the evolution of average total
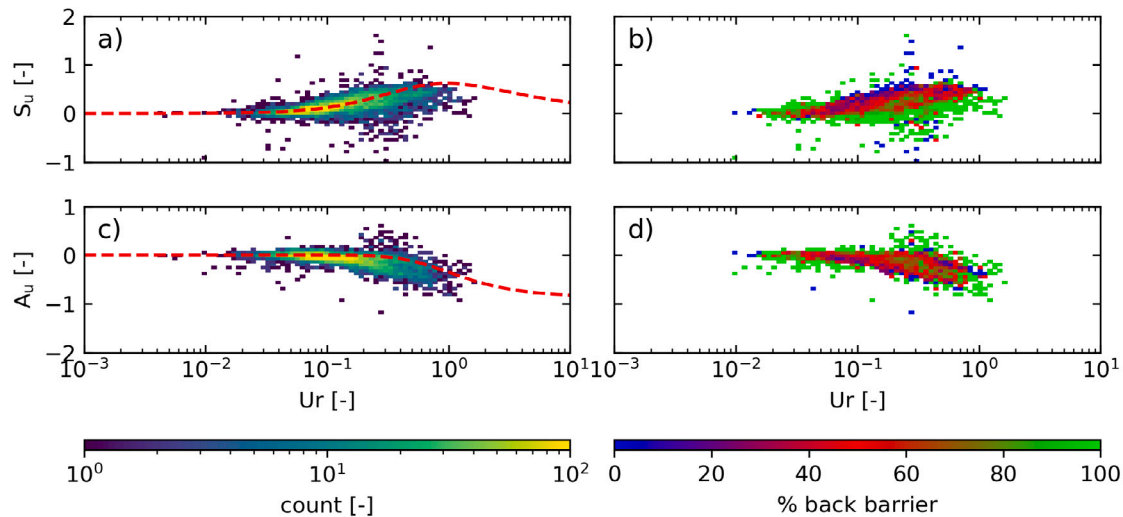
Fig. 5. Phase relation between S_u and A_u and nonlinearity parameter Ursell (Ur) on log-linear scale. (a) 2D Histogram of S_u as function of Ursell, (b) Percentage of observations attributed to the back-barrier dataset within histogram pixel in panel (a) (i.e. 100% back-barrier in green, 100% lakeside in blue), (c) 2D-Histogram of A_u as a function of Ur, (d) Percentage of observations attributed to the back-barrier dataset per pixel in panel (c). The RRvR12 parametrization is added in (a) and (c) for reference with a red dashed line.
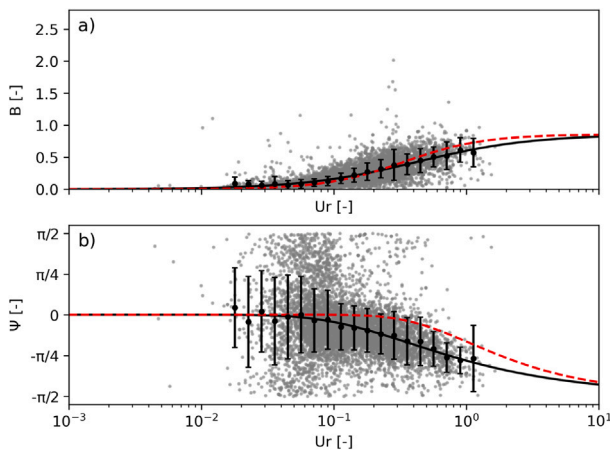

Fig. 6. Phase plane of Ursell number versus (a) Nonlinearity magnitude B and (b) Phase Ψ for DS on log-linear scale. Observations are plotted in grey dots, class-binned mean values are plotted using black dots with error bar indicating class standard deviation. The RRvR12 fit is added in a red dashed line for reference, to be compared with the best fit for DS displayed in solid black line.

Table 1
Best-fit parameters with confidence interval for Eqs. (6) and (7) from Ruessink et al. (2012) (RRvR12), our sheltered beach dataset (DS), and the subsets of exposed and sheltered wave records DS_{sub} and DE_{sub} discussed in Section 3.4.

	p_3	p_4	p_5	p_6
RRvR12	-0.471 ± 0.025	0.297 ± 0.021	0.815 ± 0.055	0.672 ± 0.073
DS	-0.37 ± 0.03	0.43 ± 0.02	0.47 ± 0.02	0.51 ± 0.03
DS_{sub}	-0.42 ± 0.02	0.35 ± 0.01	0.44 ± 0.02	0.57 ± 0.06
DE_{sub}	-0.53 ± 0.02	0.36 ± 0.01	0.51 ± 0.02	0.78 ± 0.09

All resulting free parameters fitted on DS differ from the RRvR12 fit (Table 1). Neither for p_3 nor for p_4 (together describing the onset $B > 0$ and curvature of B between 0 and p_2) does the confidence interval for best-fit values overlap between RRvR12 and our fit on the DS data, however the separation is small. This implies that the onset of nonlinearity and the increase of B with Ursell do not differ much from RRvR12 in the range of Ursell that we have observations on. Parameters p_5 and p_6 (together describing the onset $\Psi < 0$ and curvature of Ψ between 0 and $-\frac{\pi}{2}$) were fitted with narrow confidence intervals on our dataset DS, and these confidence intervals are separated well from those in the RRvR12 fit. Because of the highly nonlinear nature of Eq. (7), the effect of changes in p_5 and p_6 could not be interpreted independently.

3.3. Goodness of fit

Although Ur describes general trends in A_u and S_u, the scatter of individual wave records around this trend is considerable. We quantified whether the spread in observed S_u and A_u around the general trend predicted by Ur is comparable between DS and DE by comparing predicted and observed S_u and A_u (Fig. 7a, b, d, e). The comparison was made for dimensional variables: $S_{u,d} = SD(u_{orb})^3 S_u$, $A_{u,d} = SD(u_{orb})^3 A_u$, as it is the dimensional velocity nonlinearity that is relevant for sediment transport. The skill of the predictor was assessed through bias, standard error (S) and mean average percentage error (MAPE) for all wave records where $|S_{u,d}|$ and $|A_{u,d}|$ were different from zero (i.e. > 0.001 (m/s)^3):

$$bias = \frac{1}{N}\sum_{i=1}^{N}(\hat{x} - x) \tag{13}$$

$$S = \frac{1}{N}\sqrt{\sum_{i=1}^{N}(\hat{x} - x)^2} \tag{14}$$

nonlinearity B (Eq. (6)) and phase Ψ (Eq. (7)). To quantify the observed difference in onset of velocity asymmetry as a function of Ur between DS and RRvR12, the free parameters p_3-p_6 from Eqs. (6) and (7) were refitted and compared to the RRvR12 fit. Parameter p_2 was not refitted on the sheltered beach dataset, as no observations were made at $Ur > 5$. Therefore, the appropriateness of the upper bound to B could not be evaluated from our dataset and it was set at $p_2 = 0.857$, equal to Ruessink et al. (2012). Prior to refitting, the observations in DS were class-binned. Then p_3-p_6 were fitted on the class-means with a nonlinear least-squares fitting procedure. The observed spread within each class was incorporated in the fitting procedure as a standard deviation of errors (Fig. 6).

In-class spread (indicated by the vertical black lines representing ± one standard deviation around the class-mean in Fig. 6) in total nonlinearity B is relatively uniform over the Ursell axis. The in-class spread in phase Ψ is largest for small Ursell values. This is to be expected because wave records with small nonlinearity B corresponding to near-linear waves have negligible skewness and asymmetry. In that case the phase Ψ is expected to be randomly distributed between $-\pi$ and π consistent with a gaussian sea-state.
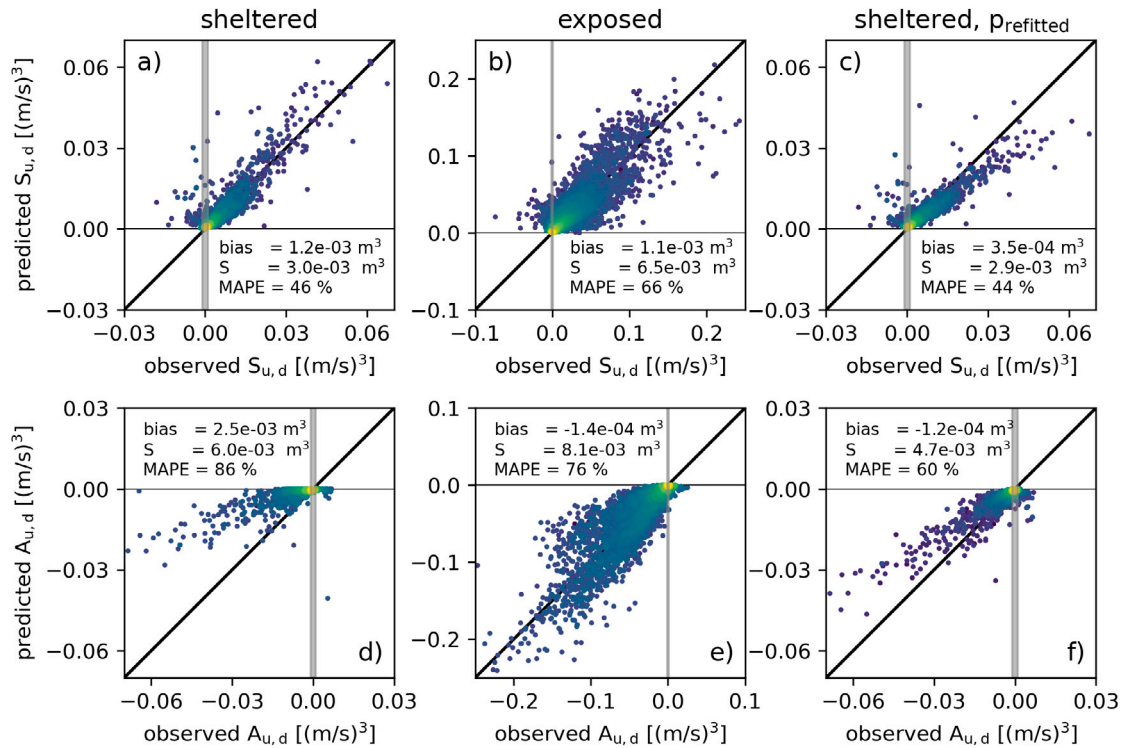
Fig. 7. Skill of dimensional wave shape prediction with an Ursell based predictor. Comparison between observed and predicted orbital velocity skewness (a–c) and orbital velocity asymmetry (d–f), all coloured by density on log scale. Panel (a) and (d) use the RRvR12 parameterization on DS. Panel (b) and (e) use the RRvR12 parameterization on DE. Panel (c) and (f) evaluate the refitted parameterization on DS. Grey vertical bands indicate observations excluded from the skill metrics due to negligible nonlinearity ($|S_u| < 0.001$ $(m/s)^3$ and $|A_u| < 0.001$ $(m/s)^3$). Skill scores are printed for the set of observations outside these bands.

$$\text{MAPE} = 100\% \cdot \frac{1}{N} \sqrt{\sum_{i=1}^{N} \frac{(\hat{x} - x)^2}{x^2}} \qquad (15)$$

where $x \in \{S_{u,d}, A_{u,d}\}$ and N the total number of wave records in the set with $|x| > 0.001$.

Using the RRvR12 parameterization on DS, $S_{u,d}$ was predicted with a MAPE of 46%, $S = 3.0e-3$ $(m/s)^3$ and bias of $1.2e-3$ $(m/s)^3$ and A_u with MAPE of 86%, $S = 6.0e-3$ $(m/s)^3$ and bias of $2.5e-3$ $(m/s)^3$ (Fig. 7a, d). Using RRvR12 on DE, $S_{u,d}$ was predicted with MAPE of 66%, $S = 6.5e-3$ $(m/s)^3$ and bias of $1.1e-3$ $(m/s)^3$ and $A_{u,d}$ with MAPE of 76%, $S = 8.1e-3$ $(m/s)^3$ and bias of $-1.4e-4$ $(m/s)^3$ (Fig. 7b, d). This shows that although the Ursell number has skill in predicting mean trends in A_u and S_u (Table 1), it does not perform that well in predicting the wave shape of individual wave records. The fact that RRvR12 does not predict the general trend in onset of asymmetry correctly for DS is only weakly visible from the MAPE in the slightly larger value for DS in comparison to DE. This shows that other processes not included in Ur affect the nonlinearity development too, both for sheltered as well as exposed wave records.

Lastly, the skill of the refitted parameterization for predicting dimensional $S_{u,d}$ and $A_{u,d}$ was evaluated. With refitted parameters (Table 1), $S_{u,d}$ was predicted with MAPE of 44%, $S = 2.9e-3$ $(m/s)^3$ and bias of $3.5e-4$ $(m/s)^3$ and $A_{u,d}$ was predicted with MAPE of 60%, $S = 4.7e-3$ $(m/s)^3$ and bias of $-1.2e-4$ $(m/s)^3$ (Fig. 7c,f). The bias in $A_{u,d}$ was reduced by an order of magnitude with refitted parameters, while the skill in predicted $S_{u,d}$ remained largely unaffected.

RRvR12 therefore predicts S_u with as much skill on our sheltered beaches as on the exposed ones. The bias in predicted $A_{u,d}$ is however large compared to observed $A_{u,d}$ when the parameters p_5 and p_6 are not refitted. This confirms, from dimensional instead of dimensionless analysis, that the trend in onset of nonlinearity is not captured well by RRvR12 for our sheltered beach observations. In the next subsections, we explore potential causes of the difference in onset of Ψ between DS and DE.

3.4. Wave steepness

The sea state of DS differed greatly from DE in its wave steepness distribution (Fig. 4). Directional spread, narrow-bandedness and relative water depth were not seen to differ substantially between DS and DE and therefore not further explored as a cause for earlier onset of Ψ. We analysed DS in subsets of equal $s_{m-1,0}$, but no clear dependence of onset of Ψ on $s_{m-1,0}$ could be discerned. We further explored the role of steepness by making a decomposition of DE, a dataset in which the interdependence of local forcing and bed geometry is believed to be smaller. From DE, a steep wave subset was selected based on the criterion $s_{m-1,0} > 0.035$, and is further referred to as DE_{sub}. DE_{sub} contains 8% of the wave records in DE. A subset of DS, further referred to as DS_{sub}, with an equal lower limit of $s_{m-1,0} > 0.035$ and an upper limit equal to highest observed steepness in DS of $s_{m-1,0} < 0.07$ was selected to compare to DE_{sub} (see Fig. 10c, f for choice of the selected steepness interval). DS_{sub} contains 47% of the wave records in DS.

In particular for the exposed subset, the subset has a different wave height distribution as all records with $H_{m0} < 0.5$ m are not part of DE_{sub} (Figs. 4a and 8a). Directional spreading in DE_{sub} is more narrow around $s_\theta = 20°$. The distribution of the mean wave period, the relative water depth and spectral bandwidth remained roughly equal after taking the wave steepness subsets.

For both DE_{sub} and DS_{sub}, the class mean and their best fit were computed (Table 1). Similar to behaviour seen in DS, Ψ onset is at lower Ur compared to RRvR12 in DE_{sub} too, although not at equal Ur as in DS_{sub}. In DE_{sub}, the Ψ onset is at approximately $Ur = 0.2$ (Fig. 9a), while in DS_{sub}, the Ψ onset is at $Ur \sim 0.1$, comparable to the onset in the entire DS. This shows that, in a mixture of many variables of influence, wave steepness is an identifier for waves that are more asymmetric than skewed. For both DS_{sub} and DE_{sub}, the relation between B and Ur remained comparable to RRvR12 (Fig. 9a and b).
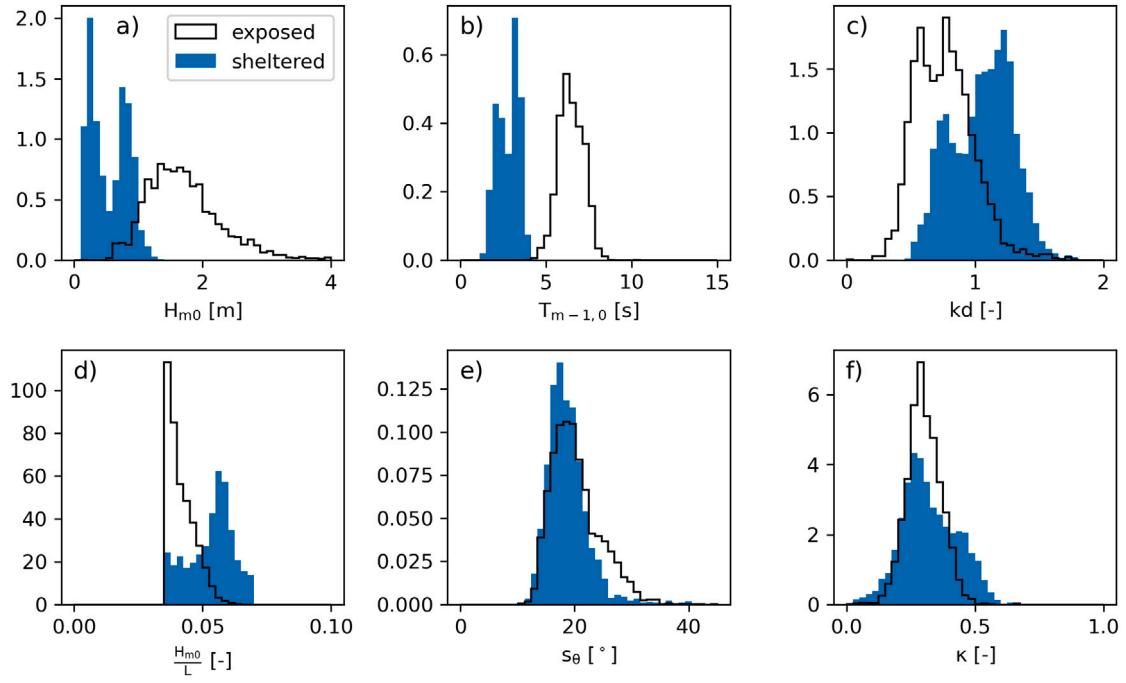
Fig. 8. Normalized (unit surface area) histograms of wave characteristics of the reduced datasets DE_{sub} (black, open) and DS_{sub} (blue filled) which are selected on the wave steepness band $0.035 \leq s_{m-1,0} < 0.07$ (see panel d), to be compared to Fig. 4. (a) Significant wave height, (b) Mean wave period $T_{m-1,0}$, (c) Relative water depth kd, (d) Local wave steepness ($s_{m-1,0}$), (e) Directional spreading, (f) Spectral narrowness κ.
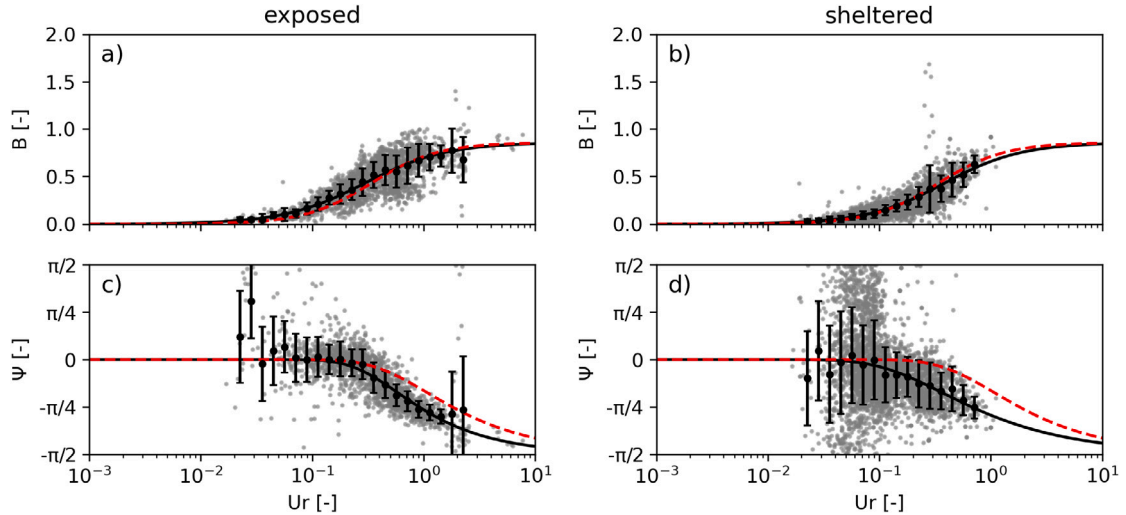

Fig. 9. Phase plane of Ursell number versus nonlinearity magnitude B (a, b) and phase Ψ (c, d) for DE_{sub} (a, c) and DS_{sub} (b, d). Observations in grey dots, class binned mean values with errorbar in black dots. The RRvR12 fit in red dashed line for reference, to be compared with the best fit in black dashed line.

3.5. Local wind

As sheltered beaches have young sea states, wave statistics are expected to correlate to prevailing winds and this opens up the possibility to study the effect that wind forcing has on wave nonlinearity. At the lakeside field site, wave height and mean period are seen to directly relate to the wind component in the wave direction (Fig. 10a, b). Unlike the lakeside beach, the back-barrier beach is not oriented in line with the dominant wind direction in the wind climate. Therefore, at the back-barrier beach, such a direct relation between wind speed and wave height is only present in moments where the wind direction is onshore. Even under offshore or strongly oblique wind directions, onshore propagating waves are recorded near the beach (Fig. 10d, e). In fact, $T_{m-1,0}$ increases with increasing opposing wind

speed as a result of waves propagating through the nearby Marsdiep tidal inlet from the North Sea which then refract towards the beach. These waves have small amplitudes but longer wave periods than the locally generated wind sea. For both sites, for following winds, wave steepness increases with wind speed too. At the lakeside beach, two patterns are identified in the phase plane of wave steepness versus wind speed (Fig. 10c). These are associated to a different response of the two deepest ADV stations, which show a steady increase from $s_{m-1,0} \approx 0.05$ to $s_{m-1,0} \approx 0.07$ for $u_{w,\parallel}$ growing from 10 m/s to 20 m/s. Wave steepness at the shallowest station, positioned right on top of the platform edge, increases at a much higher rate with $u_{w,\parallel}$, with steepness up to 0.125 observed (Fig. 10c). At the back-barrier beach, the number of observations with higher wind speeds is sparse limiting the highest steepness to $u_{w,\parallel} = 5$ m/s.
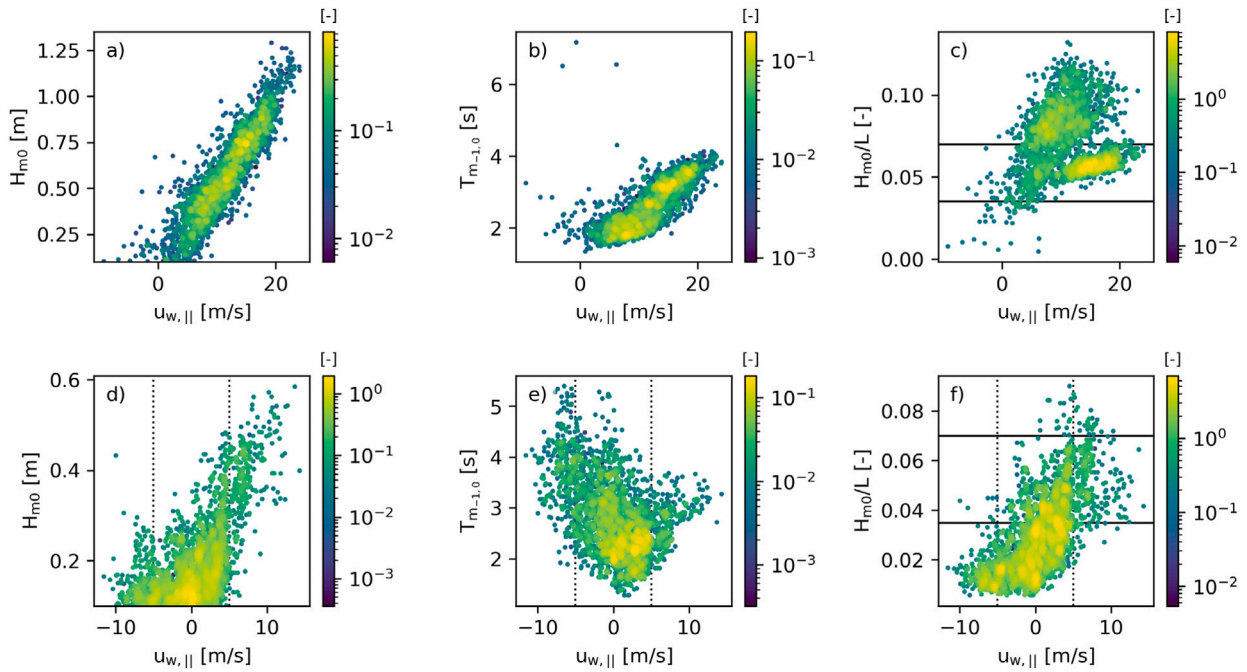
Fig. 10. Alignment of the sea state with local wind. The lakeside sea state plotted in (a–c) and the back-barrier sea state in (d–f). Phase plane of following wind speed $u_{w,\parallel}$ versus significant wave height H_{m0} in a,d, mean wave period $T_{m-1,0}$ in b,e and wave steepness $s_{m-1,0}$ in c,f. Scatter points are coloured by normalized point-density on log scale. Positive (negative) $u_{w,\parallel}$ values indicate the parallel component of the wind to the wave direction is following (opposing).
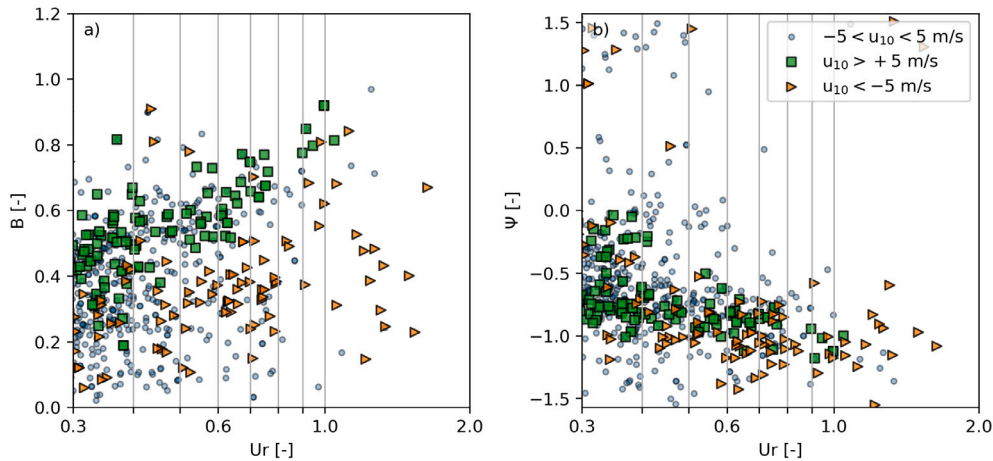

Fig. 11. The effect of following and opposing wind on the observed nonlinearity of the orbital velocities at the back-barrier dataset. The effect of wind on (a) the phase plane of B versus Ursell-B and (b) the phase plane of Ψ versus Ursell.

The effect of local wind forcing on velocity nonlinearity in DS is further examined for the back-barrier subset, as at this site there are sufficient observations with opposing wind speed while $H_{m0} > 0.1$ to compare with the following winds. Wave records were divided into three subclasses: $u_{w\parallel} < -5$ m/s (wind direction is opposing wave direction), $-5 < u_{w\parallel} < 5$ m/s and $u_{w\parallel} > 5$ m/s (wind direction is following the wave direction) and analysed for Ur after onset of nonlinearity, i.e. for $Ur > 0.3$. From this classification, it is observed that B is systematically higher for conditions with following winds (Fig. 11a). This is true for all values of $Ur > 0.3$. The scatter in B is widest for the wave records with only limited wind speed in the wave direction ($-5 < u_{w\parallel} < 5$ m/s). The dependency of Ψ on Ur does not differ between the three subclasses (Fig. 11b). This shows that in our observations, wind affects the total magnitude of wave nonlinearity, but it does not affect the phase between skewness and asymmetry.

4. Discussion

We observed that high wave steepness is an identifier for wave records in DE that, similar to DS, develop more asymmetry and less skewness than predicted trough RRvR12, while the total nonlinearity B is predicted well by RRvR12. The field data analysed in this study cannot reveal the physical relationship between steepness and the onset in nonlinearity of the orbital velocities. Both $Ur = \mathcal{F}(H, T, d)$ and $H_{m0}/L = \mathcal{F}(H, T, d)$ and therefore changes in both parameters are closely interrelated. Therefore, it can only be expected that, with considerable change in the sample population of the latter, the dependence of nonlinearity on Ur might deviate too. This is because there is no physical reason underlying the onset of RRvR12 at $Ur = 0.5$ instead of $Ur = 0.1$ either, which inhibits a physical interpretation. Here, we expand on other physical causes that might influence why the sheltered beach wave records behave more like a bore (more asymmetric) than a Stokes wave (more skewed).

4.1. Foreshore slope

The foreshore of the two beaches analysed in this study is not appropriately characterized by a single value of the cross-shore beach slope. Along the steep beach face, slopes were up to 1:8, a large beach slope that was not captured in the exposed coastal dataset (containing data from sites with foreshores gentler than 1:20, but with considerable sand bars). At the same time, a near-horizontal subtidal platform was present at both sheltered beaches. Nonhydrostatic numerical simulations by Rocha et al. (2017) and Filipot (2015) showed that wave nonlinearity is less pronounced (lower B) on steeper slopes. Indeed, Fig. 6a hints towards underestimation of B in our dataset compared to RRvR12. Because DS contains no wave records with $Ur > 3$, the value of p_2 (being the upper bound to B) could not be evaluated from this dataset and we cannot draw any definitive conclusions on this potential relation. The steep bottom slope could also be considered a cause of the earlier onset of Ψ. However, both the central lakeside ADV station on the steep slope and the deepest back-barrier ADV station on the near-horizontal platform, did not have any wave records with wave asymmetry while Ur reached 0.3. This suggests that bottom slope may play a role through cumulative wave breaking history (De Wit et al., 2019), but the local bottom slope by itself is not an indicator of the early onset of Ψ.

As shown by Rocha et al. (2013, 2017), nonlocal information from the system, such as the average beach slope or the offshore wave steepness can be added as dependent variables to a wave nonlinearity predictor. While they showed that adding this nonlocal information improved predictive skill, these additions complicate the use of such predictors in morphodynamic models. Offshore boundary conditions and the bathymetry need not be uniform for the entire model domain, so the deep water conditions corresponding to an arbitrary interior point on the domain are not readily available without reversing the wave action balance. Therefore, the benefit of these additions is not further assessed here.

There are other dependencies identified in the literature that affect wave nonlinearity. Ruessink et al. (2012) and Rocha et al. (2017) report seeing a dependency of skewness on directional spread in their dataset. This was particularly apparent for small directional spreading values ($s_\theta < 10°$), and analysed for high Ursell number $Ur \in [0.75–2]$. We did not observe such a dependency in our data. Potentially, this is caused by the limited data coverage for small directional spreads: our data (the entire datasets, not only the subset DS) only contains 15 wave records with directional spread of 15° or less, at Ursell number above 0.75. At larger directional spreading values above 15°, the dependency of skewness shown in the literature was weak too.

4.2. Effect of local wind forcing

We showed that in the back-barrier dataset, local wind forcing increases total wave nonlinearity B, but did not affect phase Ψ. From this field dataset, it was impossible to vary wind speed, but keep other dependent variables entirely constant. By class-binning the back-barrier observations in 3 wind speed categories, implicitly we also co-varied wave height and steepness (Fig. 10d, f). These two sea state statistics explained less of the variance in B than following wind-speed did.

Laboratory experiments in deep water to intermediate water showed that mainly asymmetry is increased by following wind speed (Leykin et al., 1995). Later experiments showed that for shoaling waves both skewness and asymmetry are increased with increasing following wind speed (Feddersen and Veron, 2005). Our data showed both velocity skewness and asymmetry are enhanced by following winds, but their ratio is unaffected. Although this observed increase in B is in line with the results near the breakpoint in Feddersen and Veron (2005) and the recent theoretical considerations for shallow water wave shape by Zdyrski and Feddersen (2021), their analysis did not explicitly suggest the independence of Ψ on wind forcing. There are several

factors that complicate a direct comparison of their lab findings to our field observations. First, the lab studies investigated the shape of monochromatic waves while our observations are from random sea states. Moreover, our data span a much wider range of inverse wave age ($\frac{u_{w,\parallel}}{c} \in [0, 40]$ for the wave records in Fig. 11), while work by Leykin et al. (1995) was limited to $\frac{u_{w,\parallel}}{c} \in [0, 2]$ and Feddersen and Veron (2005) discussed $\frac{u_{w,\parallel}}{c} \in [0, 8]$. Our analysis adds to earlier studies by examining field data for the relationship between wind and nonlinearity and by showing that including wind helps to explain the observed spread in B as function of Ur.

4.3. Implications for sediment transport modeling

The key observation from our analysis for the application of engineering type sediment transport models at sheltered beaches is that both skewness and asymmetry develop as a function of Ursell number. Moreover, the predictive skill of the Ursell-based predictor for nonlinearity magnitude B is comparable to exposed coast beaches on which the predictor has shown skill in morphodynamic modeling (Sherwood et al., 2022).

Whether or not the observed difference in onset of nonzero phase between skewness and asymmetry is relevant for modelling sediment transport, relies in part on the physical rationale of the chosen sediment transport formulation. Here we focus on those formulations that explicitly include both skewness and asymmetry, as both are key for onshore sediment transport (Hoefel and Elgar, 2003; Drake and Calantoni, 2001) and are included in most state-of-the-art engineering models (Van der Werf et al., 2015; Zheng et al., 2023; Kalra et al., 2019; Shafiei et al., 2023; van Thiel de Vries, 2009).

Under energetic conditions, when transport occurs in the sheetflow regime, the direction of skewness and asymmetry driven fluxes are both onshore directed (Henderson et al., 2004; Hsu et al., 2006; Dubarbier et al., 2015). This could imply that it is sufficient to only resolve the total nonlinearity driven transport instead of skewness and asymmetry driven separately (e.g. Ruessink et al., 2007). The advantage of treating skewness and asymmetry driven onshore transport separately in engineering type morphodynamic models is that it enables a differentiation in process strength between intermediate water depths (skewed-only waves) and the inner surf zone (both skewed and asymmetric waves), which enhances the skill of calibrated models over very mildly sloping beaches that cover both stormy and calm conditions (Bouchat Albernaz et al., 2019). The relative strength of skewness or asymmetry in engineering type transport models is largely determined by the tuning of calibration coefficients that determine the balance between nonlinearity driven sediment transport to other transport components. Therefore, while adjusting $p_2 - p_6$ may be relevant in more accurately predicting wave-shape evolution on sheltered beaches, it has to be kept in mind that the magnitude of the onshore sand transport also depends on additional calibration coefficients.

In the less energetic vortex ripple regime, wave nonlinearity driven transport can be either onshore or offshore directed, as a result of phase-lag effects between ripple lee-side vortices and sediment concentrations. Models incorporating this regime transition are able to differentiate between onshore directed and offshore directed wave-driven sediment fluxes (Van der A et al., 2013; Van Rijn et al., 2013). Over a rippled bed the phase between skewness and asymmetry can be paramount for a correct prediction of the net transport direction, as laboratory measurements showed that asymmetric, but hardly skewed near-bed velocity led to a onshore directed suspended flux, while skewed and asymmetric near-bed velocities result in offshore suspended fluxes (Van der Zanden et al., 2017; Fritsch et al., 2024). This delicate balance between ripple geometry and wave nonlinearity is currently unresolved in engineering type morphodynamic models, and considering the spread in observed skewness and asymmetry for a given Ursell number (Fig. 5) it is unlikely that an Ursell based predictor will have skill in predicting this flux reversal.

Therefore, these observations validate the application of RRvR12 on sheltered beaches, inasmuch as the prevailing transport regime is resolved by the transport formulations used. By applying RRvR12, a model will correctly account for the general trend in development of nonlinearity magnitude B, which combined with state-of-the-art transport models, describes spatial gradients in onshore sediment transport in the cross-shore. Whether engineering type morphodynamic models can describe the net transport direction well over rippled beds is beyond the scope of this work and a topic for further research.

5. Conclusion

This study investigated near-bed orbital velocity nonlinearity from wave records collected at two sheltered beaches, a beach type not part of the well-used predictor RRvR12 derived by Ruessink et al. (2012). The sheltered beaches studied are characterized by a low-energy sea state arriving on a narrow and steep beach face. The Ursell number was shown to be a good indicator for nonlinearity at sheltered beaches. Velocity asymmetry in the sheltered dataset onsets at lower Ursell numbers than predicted by RRvR12. From the sheltered dataset alone we could not determine the driver for this earlier onset. However, comparison of the sheltered dataset to exposed coast observations that were part of Ruessink et al. (2012) revealed that the low-energy wave records have much higher wave steepness ($s_{m-1,0} > 0.035$) than a typical exposed coastal wave record. A decomposition of the exposed dataset into mild and steep wave records revealed that in this dataset too, the steep wave records are more asymmetric than predicted through RRvR12.

Although the Ursell number predicts general trends in development of wave nonlinearity, it makes errors in the order of 50% in predicting the shape of individual wave records. This is not unique to our sheltered beach dataset but was seen to hold for individual wave records of the exposed coastal dataset too. This stresses again that Ur does not capture all processes involved that result in an individual record of nonlinearity. Using the back-barrier wave records, following wind was shown to positively correlate to the magnitude B of total velocity nonlinearity, while Ψ remained unaffected by local following or opposing wind speed. Including wind direction in the analysis of field observations of wave nonlinearity aids the interpretation of observed spread in total nonlinearity.

Refitting the free parameters of an Ursell based predictor on the sheltered wave records was shown to reduce the bias between predicted and observed dimensional asymmetry $A_{u,d}$, but it should be kept in mind that the magnitude of wave-nonlinearity-driven sediment transport in engineering scale modelling of sheltered beaches morphodynamics depends on additional calibration coefficients too.

CRediT authorship contribution statement

M.A. van der Lugt: Writing – original draft, Methodology, Formal analysis, Data curation, Conceptualization. **M.A. de Schipper:** Writing – review & editing, Supervision, Methodology, Funding acquisition, Conceptualization. **A.J.H.M. Reniers:** Writing – review & editing, Supervision, Methodology. **B.G. Ruessink:** Writing – review & editing, Methodology.

Declaration of competing interest

The authors declare that they have no known competing financial interests or personal relationships that could have appeared to influence the work reported in this paper.

Data availability

Data from the back-barrier field site are part of the SEDMEX collection, available at the 4TU data repository at https://data.4tu.nl/collections/19c5676c-9cea-49d0-b7a3-7c627e436541. Data from the lakeside field site are part of the Houtribdijk Lakeside campaign. These data are available at the Rijkswaterstaat data repository at https://waterinfo-extra.rws.nl/projecten/%40205186/versterking. The data from the exposed coast sites are available from the authors upon request.

Acknowledgements

References

Bailard, J.A., Inman, D.L., 1981. An Energetics Bedload Model for a Plane Sloping Beach: Local Transport. J. Geophys. Res.: Oceans 86, 2035–2043. http://dx.doi.org/10.1029/JC086iC03p02035.

Battjes, J.A., van Vledder, G.P., 1984. Verification of Kimura's theory for wave group statistics. In: Proceedings of the 19th International Conference on Coastal Engineering. ASCE, Houston, Texas, United States, pp. 641–648.

Bouchat Albernaz, M., Ruessink, B., Jagers, H., Kleinhans, M., 2019. Effects of Wave Orbital Velocity Parameterization on Nearshore Sediment Transport and Decadal Morphodynamics. J. Mar. Sci. Eng. 7 (188), http://dx.doi.org/10.3390/jmse7060188.

De Wit, F., Tissier, M., Reniers, A., 2019. Characterizing Wave Shape Evolution on an Ebb-Tidal Shoal. J. Mar. Sci. Eng. 7 (367), http://dx.doi.org/10.3390/jmse7100367.

Doering, J., Bowen, A., 1995. Parametrization of orbital velocity asymmetries of shoaling and breaking waves using bispectral analysis. Coast. Eng. 26, 15–33. http://dx.doi.org/10.1016/0378-3839(95)00007-X.

Donelan, M., Hamilton, J., Hui, W., 1985. Directional spectra of wind generated waves. Directional spectra of wind-generated ocean waves. Philos. Trans. R. Soc. Lond. Ser. A Math. Phys. Sci. 315, 509–562.

Drake, T.G., Calantoni, J., 2001. Discrete particle model for sheet flow sediment transport in the nearshore. J. Geophys. Res.: Oceans 106, 19859–19868. http://dx.doi.org/10.1029/2000JC000611.

Dubarbier, B., Castelle, B., Marieu, V., Ruessink, G., 2015. Process-based modeling of cross-shore sandbar behavior. Coast. Eng. 95, 35–50. http://dx.doi.org/10.1016/j.coastaleng.2014.09.004.

Duran-Matute, M., Gerkema, T., Sassi, M.G., 2016. Quantifying the residual volume transport through a multiple-inlet system in response to wind forcing: The case of the western Dutch Wadden Sea: WIND FORCING IN MULTI-INLET SYSTEM. J. Geophys. Res.: Oceans 121, 8888–8903. http://dx.doi.org/10.1002/2016JC011807.

Elgar, S., Guza, R.T., 1985. Shoaling gravity waves: Comparisons between field observations, linear theory, and a nonlinear model. J. Fluid Mech. 158, 47–70. http://dx.doi.org/10.1017/S0022112085002543.

Ewans, K.C., 1998. Observations of the Directional Spectrum of Fetch-Limited Waves. J. Phys. Oceanogr. 28, 495–512. http://dx.doi.org/10.1175/1520-0485(1998)028<0495:OOTDSO>2.0.CO;2.

Feddersen, F., Veron, F., 2005. Wind Effects on Shoaling Wave Shape. J. Phys. Oceanogr. 35, 1223–1228. http://dx.doi.org/10.1175/JPO2753.1.

Fellowes, T.E., Vila-Concejo, A., Gallop, S.L., Schosberg, R., de Staercke, V., Largier, J.L., 2021. Decadal shoreline erosion and recovery of beaches in modified and natural estuaries. Geomorphology 390, 107884. http://dx.doi.org/10.1016/j.geomorph.2021.107884.

Filipot, J.F., 2015. Investigation of the Bottom-Slope Dependence of the Nonlinear Wave Evolution toward Breaking Using SWASH. J. Coast. Res. 32, 1504. http://dx.doi.org/10.2112/JCOASTRES-D-15-00118.1.

Fritsch, N., Fromant, G., Hurther, D., Cáceres, I., 2024. Coarse Sand Transport Processes in the Ripple Vortex Regime Under Asymmetric Nearshore Waves. J. Geophys. Res.: Oceans 129, e2023JC020189. http://dx.doi.org/10.1029/2023JC020189.

Guo, J., 2002. Simple and explicit solution of wave dispersion equation. Coast. Eng. 4.

Henderson, S.M., Allen, J.S., Newberger, P.A., 2004. Nearshore sandbar migration predicted by an eddy-diffusive boundary layer model. J. Geophys. Res.: Oceans 109, 2003JC002137. http://dx.doi.org/10.1029/2003JC002137.

Hoefel, F., Elgar, S., 2003. Wave-Induced Sediment Transport and Sandbar Migration. Science 299, 1885–1887. http://dx.doi.org/10.1126/science.1081448.

Hsu, T.J., Elgar, S., Guza, R., 2006. Wave-induced sediment transport and onshore sand-bar migration. Coast. Eng. 53, 817–824. http://dx.doi.org/10.1016/j.coastaleng.2006.04.003.

Jackson, N.L., Nordstrom, K.F., Eliot, I., Masselink, G., 2002. 'Low energy' sandy beaches in marine and estuarine environments: A review. Geomorphology 48, 147–162. http://dx.doi.org/10.1016/S0169-555X(02)00179-4.

Kalra, T.S., Sherwood, C.R., Warner, J.C., Rafati, Y., Hsu, T.J., 2019. Investigating Bedload Transport Under Asymmetrical Waves Using a Coupled Ocean-Wave Model. In: Coastal Sediments 2019. WORLD SCIENTIFIC, Tampa/St. Petersburg, Florida, USA, pp. 591–604. http://dx.doi.org/10.1142/9789811204487_0052.

Kalra, T.S., Suttles, S.E., Sherwood, C.R., Warner, J.C., Aretxabaleta, A.L., Leavitt, G.R., 2022. Shoaling Wave Shape Estimates from Field Observations and Derived Bedload Sediment Rates. J. Mar. Sci. Eng. 10 (223), http://dx.doi.org/10.3390/jmse10020223.

KNMI, KNMI uurgegevens Houtribdijk.

Kroon, A., De Boer, A., 2001. Horizontal Flow Circulation on a Mixed Energy Beach. In: Coastal Dynamics '01. American Society of Civil Engineers, Lund, Sweden, pp. 548–557. http://dx.doi.org/10.1061/40566(260)56.

Kuik, A., Van Vledder, G.Ph., Holthuijsen, L., 1988. A Method for the Routine Analysis of Pitch-and-Roll Buoy Wave Data. J. Phys. Oceanogr. 18, 1020–1034.

Lesser, G., Roelvink, J., Van Kester, J., Stelling, G., 2004. Development and validation of a three-dimensional morphological model. Coast. Eng. 51, 883–915. http://dx.doi.org/10.1016/j.coastaleng.2004.07.014.

Leykin, I., Donelan, M., Mellen, R., McLauglin, D., 1995. Asymmetry of wind waves studies in a laboratory tank. Nonlinear Process. Geophys. 2, 280–289.

Lygre, A., Krogstadt, H., 1986. Maximum Entropy Estimation of the Directional Distribution in Ocean Wave Spectra. J. Phys. Oceanogr. 16, 2052–2060.

Miche, R., 1944. Miche, M. Mouvements ondulatoires de la mer en profendeur constante ou décroissante. Ann. Ponts Chaussées 114, 369–406.

Perk, L., van Rijn, L., Koudstaal, K., Fordeyn, J., 2019. A Rational Method for the Design of Sand Dike/Dune Systems at Sheltered Sites; Wadden Sea Coast of Texel, The Netherlands. J. Mar. Sci. Eng. 7, 324. http://dx.doi.org/10.3390/jmse7090324.

Price, T., Ruessink, B., 2008. Morphodynamic zone variability on a microtidal barred beach. Mar. Geol. 251, 98–109. http://dx.doi.org/10.1016/j.margeo.2008.02.008.

Rocha, M., Michallet, H., Silva, P., 2017. Improving the parameterization of wave nonlinearities – The importance of wave steepness, spectral bandwidth and beach slope. Coast. Eng. 121, 77–89. http://dx.doi.org/10.1016/j.coastaleng.2016.11.012.

Rocha, M., Silva, P., Michallet, H., Abreu, T., Moura, D., Fortes, J., 2013. Parameterizations of wave nonlinearity from local wave parameters: A comparison with field data. J. Coast. Res. 65, 374–379. http://dx.doi.org/10.2112/SI65-064.1.

Roelvink, D., Reniers, A., Van Dongeren, A., Van Thiel De Vries, J., McCall, R., Lescinski, J., 2009. Modelling storm impacts on beaches, dunes and barrier islands. Coast. Eng. 56, 1133–1152. http://dx.doi.org/10.1016/j.coastaleng.2009.08.006.

Ruessink, B., Houwman, K., Hoekstra, P., 1998. The systematic contribution of transporting mechanisms to the cross-shore sediment transport in water depths of 3 to 9 m. Mar. Geol. 152, 295–324. http://dx.doi.org/10.1016/S0025-3227(98)00133-9.

Ruessink, B.G., Kuriyama, Y., Reniers, A.J.H.M., Roelvink, J.A., Walstra, D.J.R., 2007. Modeling cross-shore sandbar behavior on the timescale of weeks. J. Geophys. Res.: Earth Surf. 112, 2006JF000730. http://dx.doi.org/10.1029/2006JF000730.

Ruessink, B.G., Miles, J.R., Feddersen, F., Guza, R.T., Elgar, S., 2001. Modeling the alongshore current on barred beaches. J. Geophys. Res.: Oceans 106, 22451–22463. http://dx.doi.org/10.1029/2000JC000766.

Ruessink, B., Ramaekers, G., van Rijn, L., 2012. On the parameterization of the free-stream non-linear wave orbital motion in nearshore morphodynamic models. Coast. Eng. 65, 56–63. http://dx.doi.org/10.1016/j.coastaleng.2012.03.006.

Shafiei, H., Chauchat, J., Bonamy, C., Marchesiello, P., 2023. Adaptation of the SANTOSS transport formula for 3D nearshore models: Application to cross-shore sandbar migration. Ocean Model. 181, 102138. http://dx.doi.org/10.1016/j.ocemod.2022.102138.

Sherwood, C.R., Van Dongeren, A., Doyle, J., Hegermiller, C.A., Hsu, T.J., Kalra, T.S., Olabarrieta, M., Penko, A.M., Rafati, Y., Roelvink, D., Van der Lugt, M., Veeramony, J., Warner, J.C., 2022. Modeling the Morphodynamics of Coastal Responses to Extreme Events: What Shape Are We In? Annu. Rev. Mar. Sci. 14, 457–492. http://dx.doi.org/10.1146/annurev-marine-032221-090215.

Ton, A.M., 2023. SAndy Beaches in Low-Energy (Ph.D. thesis). Delft University of Technology., Delft.

Ton, A.M., Vuik, V., Aarninkhof, S.G., 2021. Sandy beaches in low-energy, non-tidal environments: Linking morphological development to hydrodynamic forcing. Geomorphology 374, 107522. http://dx.doi.org/10.1016/j.geomorph.2020.107522.

Van der A, D.A., Ribberink, J.S., van der Werf, J.J., O'Donoghue, T., Buijsrogge, R.H., Kranenburg, W.M., 2013. Practical sand transport formula for non-breaking waves and currents. Coast. Eng. 76, 26–42. http://dx.doi.org/10.1016/j.coastaleng.2013.01.007.

Van der Lugt, M.A., Bosma, J.W., De Schipper, M.A., Price, T.D., Van Maarseveen, M.C.G., Van Der Gaag, P., Ruessink, G., Reniers, A.J.H.M., Aarninkhof, S.G.J., 2024. Measurements of morphodynamics of a sheltered beach along the Dutch Wadden Sea. Earth Syst. Sci. Data 16, 903–918. http://dx.doi.org/10.5194/essd-16-903-2024.

Van der Werf, J., Veen, R., Ribberink, J., Van der Zanden, J., 2015. Testing of the new SANTOSS Transport Formula in the Delft3D Morphological Modeling System. In: The Proceedings of the Coastal Sediments 2015. WORLD SCIENTIFIC, San Diego, USA, http://dx.doi.org/10.1142/9789814689977_0100.

Van der Zanden, J., Van der A, D., Hurther, D., Cáceres, I., O'Donoghue, T., Ribberink, J., 2017. Suspended sediment transport around a large-scale laboratory breaker bar. Coast. Eng. 125, 51–69. http://dx.doi.org/10.1016/j.coastaleng.2017.03.007.

Van Rijn, L.C., 2007. Unified View of Sediment Transport by Currents and Waves. II: Suspended Transport. J. Hydraul. Eng. 133, 668–689. http://dx.doi.org/10.1061/(ASCE)0733-9429(2007)133:6(668).

Van Rijn, L.C., Ribberink, J.S., Werf, J.V.d., Walstra, D.J., 2013. Coastal sediment dynamics: Recent advances and future research needs. J. Hydraul. Res. 51, 475–493. http://dx.doi.org/10.1080/00221686.2013.849297.

van Thiel de Vries, J.S.M., 2009. Dune Erosion During Storm Surges (Ph.D. thesis). Technische Universiteit Delft., Delft.

Vila-Concejo, A., Gallop, S.L., Largier, J.L., 2020. Sandy beaches in estuaries and bays. In: SAndy Beach Morphodynamics. Elsevier, pp. 343–362. http://dx.doi.org/10.1016/B978-0-08-102927-5.00015-1.

Warner, J.C., Sherwood, C.R., Signell, R.P., Harris, C.K., Arango, H.G., 2008. Development of a three-dimensional, regional, coupled wave, current, and sediment-transport model. Comput. Geosci. 34, 1284–1306. http://dx.doi.org/10.1016/j.cageo.2008.02.012.

Young, I., Verhagen, L., Khatri, S., 1996. The growth of fetch limited waves in water of finite depth. Part 3. Directional spectra. Coast. Eng. 29, 101–121. http://dx.doi.org/10.1016/S0378-3839(96)00026-9.

Zdyrski, T., Feddersen, F., 2021. Wind-induced changes to surface gravity wave shape in shallow water. J. Fluid Mech. 913 (A27), http://dx.doi.org/10.1017/jfm.2021.15.

Zheng, P., Gumbira, G., Li, M., Van der Zanden, J., Van der A, D., Van der Werf, J., Chen, X., Tang, X., 2023. Development, calibration and validation of a phase-averaged model for cross-shore sediment transport and morphodynamics on a barred beach. Cont. Shelf Res. 258, 104989. http://dx.doi.org/10.1016/j.csr.2023.104989.